crystals

MDPI

Article

Gemology, Spectroscopy, and Mineralogy Study of Aquamarines of Three Different Origins

Shiyuan Cui [1], Bo Xu [1,2,3,*], Jiaqi Shen [1], Zhuang Miao [1] and Zixuan Wang [1]

[1] School of Gemmology, China University of Geoscience Beijing, 29 Xueyuan Road, Haidian District, Beijing 100083, China; shiyuancui@email.cugb.edu.cn (S.C.); shenjiaqi0426@163.com (J.S.); zhuangmiao@cugb.edu.cn (Z.M.); wangzx@cugb.edu.cn (Z.W.)
[2] State Key Laboratory of Geological Processes and Mineral Resources, China University of Geoscience Beijing, 29 Xueyuan Road, Haidian District, Beijing 100083, China
[3] The Beijing SHRIMP Center, Chinese Academy of Geological Sciences, Beijing 100037, China
* Correspondence: bo.xu@cugb.edu.cn

Abstract: New aquamarine deposits have been found around the world in recent years, and how to compare and distinguish aquamarines of different origin has become a significant problem. Aquamarines from Koktokay, Minas Gerais, and Namaqualand were collected for standard gemology tests, spectroscopy, and chemical analysis in this paper. The spectroscopy experiment included infrared spectroscopy and Raman spectroscopy. Chemical composition analysis comprises electron microprobe and laser ablation–inductively coupled plasma–mass spectrometry (LA-ICP-MS). The results show that infrared absorption peaks related to $[Fe_2(OH)_4]$ and NaH are found in Koktokay and Minas Gerais aquamarines, respectively. Compared with other two origins, Namaqualand aquamarine have strongest type II water Raman peak related to alkali metal content. Compared with aquamarines from other sources, aquamarines from Xinjiang and Minas Gerais are characterized by relatively high aluminum and low alkali contents in chemical composition, while Namaqualand aquamarine have a high scandium content.

Keywords: beryl; aquamarine; spectroscopy; mineral chemistry; Koktokay; Minas Gerais; Namaqualand

check for updates

Citation: Cui, S.; Xu, B.; Shen, J.; Miao, Z.; Wang, Z. Gemology, Spectroscopy, and Mineralogy Study of Aquamarines of Three Different Origins. *Crystals* **2023**, *13*, 1478. http://doi.org/10.3390/cryst13101478

Academic Editor: Sergey V. Krivovichev

Received: 11 September 2023
Revised: 30 September 2023
Accepted: 9 October 2023
Published: 11 October 2023

Copyright: © 2023 by the authors. Licensee MDPI, Basel, Switzerland. This article is an open access article distributed under the terms and conditions of the Creative Commons Attribution (CC BY) license (https://creativecommons.org/licenses/by/4.0/).

1. Introduction

Beryl is one of the most common beryllium-containing minerals, and is formed only in particular geological environments. There are several types of beryllium ore deposits, but three are predominant: granitic pegmatite deposits, volcanogenic, and carbonate-hosted pegmatite deposits. These deposits are distributed throughout the world and the presence of beryl, especially in large crystals, is typically associated with granitic pegmatites [1,2].

The chemical formula of beryl is $Be_3Al_2Si_6O_{18}$. In beryl crystal, the $[Si_6O_{18}]$ hexagonal rings consist of $[SiO_4]$ tetrahedron (T1 site) arranged perpendicular to the C-axis, and a channel structure parallel to the C-axis is formed. The hexagonal rings are connected to each other by $[BeO_4]$ tetrahedra and $[AlO_6]$ octahedra [3]. In $[BeO_4]$ (T2 site), the Be^{2+} ion is mainly replaced by Li^+, and the charge deficiency from this is compensated by the entry of other alkali metal ions (Na^+, K^+, Rb^+, and Cs^+), which preferentially localize in the channel (CH site). In $[AlO_6]$ octahedrons (O site), Al^{3+} can be replaced by Fe^{3+}, Cr^{3+}, Fe^{2+}, Mn^{2+}, Ca^{2+}, and Mg^{2+}. When Al^{3+} cations are replaced by divalent cations, the charge deficiency is also compensated by the entry of alkali metal ions [4]. The channels also incorporate water molecules, which arrange themselves in two ways: type I water, with a H-H direction parallel to the C-axis, and type II water, with a H-H direction perpendicular to the C-axis (Figure 1) [5].

Based on its color, beryl is divided into different varieties, such as emerald, aquamarine, heliodor, morganite, red beryl, and goshenite [6]; in particular, the aquamarine shows a

blue color similar to that of the sea and a high transparency. As new deposits of aquamarine are continuously being discovered [2,7–9], it has become important to establish parameters to ascertain the different origins of this species when present on the market.

The spectroscopic measurements are nondestructive and can determine some basic information related to chemical composition [10]. The EMPA and LA-ICP-MS techniques are the ones mainly used for in situ mineralogical analysis [11–15], and for the determination of the origin of the gem [10,16–18]. Thus, the combination study of spectroscopic signature and chemical composition can provide more comprehensive information about the gemstone. In this study, we investigated aquamarine samples from three countries which are the most representative in terms of provenance and are commonly found in business: Xinjiang in China, Minas Gerais in Brazil, and Namaqualand in South Africa. Gemology, spectroscopy, and major and trace element analyses were performed to determine their characteristics and differences. The result of this study will provide indications for determining the properties of Xinjiang, Minas Gerais, and Namaqualand aquamarines and distinguishing their origins.

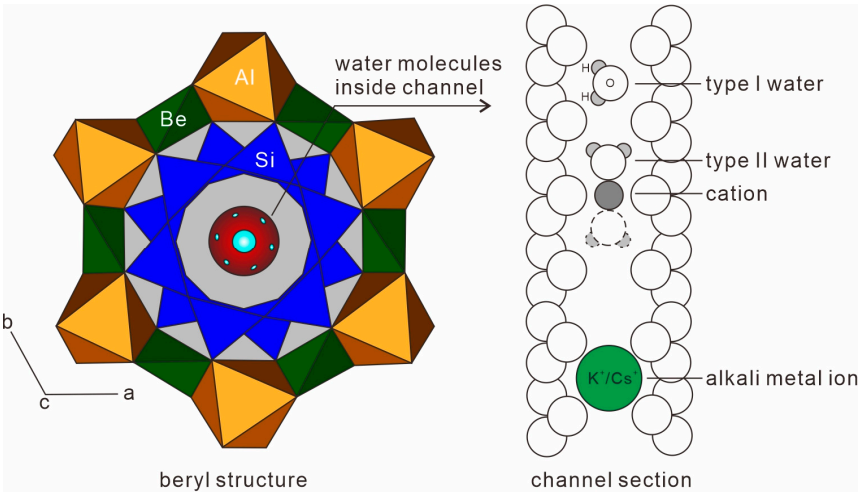

Figure 1. Beryl crystal structure and channel section, modified from [19,20].

2. Materials and Methods

Four aquamarines were selected randomly from samples of different origins for further analysis. Those four samples from Xinjiang, China (XJ-1, XJ-2), Minas Gerais, Brazil (MG), and Namaqualand, South Africa (NA) were examined using standard gemological tests, infrared spectroscopy, Raman spectroscopy, electron microprobe (EMPA), and laser ablation–inductively coupled plasma–mass spectrometry (LA-ICP-MS) (Figures 2 and 3).

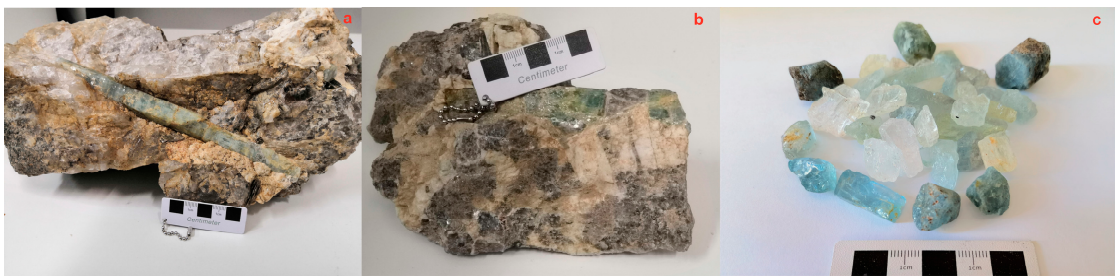

Figure 2. (**a**,**b**) Aquamarine crystals in pegmatite from Koktokay, Xinjiang (XJ-1 and XJ-2). (**c**) Aquamarine samples from multiple origins.

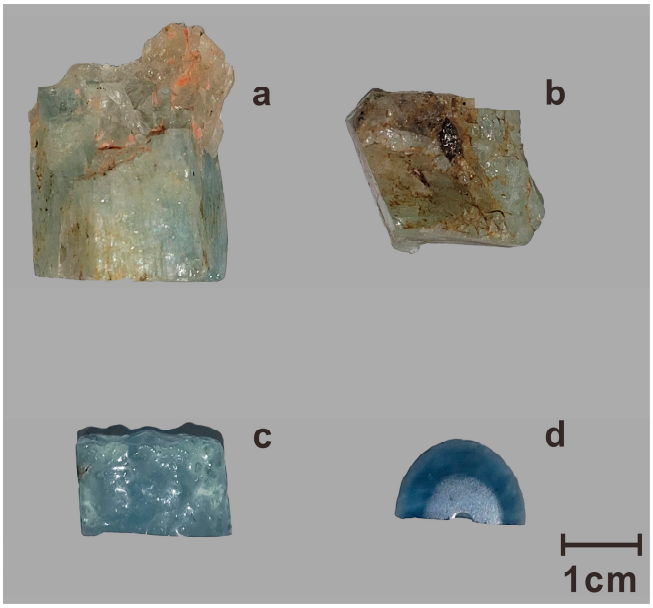

Figure 3. The four samples of aquamarine investigated in this work: (**a**) XJ-1. (**b**) XJ-2. (**c**) MG. (**d**) NA.

Aquamarines from Xinjiang were obtained from Koktokay pegmatite, which is the largest of Li-Be-Nb-Ta-Cs pegmatitic rare metal deposit of the Chinese Altai orogenic. The Koktokay pegmatite includes a metagabbro pluton, and can be classified into nine internal zones. The graphic pegmatite zone is mainly composed of microcline, albite, quartz; and muscovite. Aquamarines are a characteristic accessory mineral [21].

Minas Gerais Aquamarine was selected from Araçuai region, which is located in northern Minas Gerais states. Pegmatites with aquamarine in Araçuai region contain mostly microcline, quartz, albite, and muscovite. Two-mica leucogranites are the source of pegmatites and aquamarine is the subordinate mineral in pegmatites [22].

Namaqualand Aquamarine was collected from Noumas pegmatite; such pegmatite mainly consists of aplite border, wall zone, intermediate zone, and quartz-K-feldspar zone. Beryl is commonly found in wall zone and intermediate zone. The wall zone was mainly composed of albite, microcline, quartz, and muscovite, while quartz, microcline, and plagioclase are predominant in intermediate zone [23].

Standard gemological analyses included optical properties, ultraviolet fluorescence, and specific gravity. Refractive index (RI) and birefringence index (DR) were tested in polish surfaces of samples and measured using refractometer (Xueyuan Jewelry Technologies, Wuhan, China) Each sample was observed from different crystal direction using calcite dichroscope and Chelsea color filter (CCF) (Baoguang Technologies, Nanjing, China). Ultraviolet fluorescence (UV) was observed under ultraviolet lamp at longwave (365 nm) and shortwave (254 nm). Specific gravity (SG) was obtained using hydrostatic weighing method. Samples were weighed in air and water.

Infrared spectra were collected using Bruker Tensor 27 Fourier Infrared spectrometer with scanning time of 32 s, resolution of 4 cm^{-1}, and wavenumber between 400 and 4000 cm^{-1}. The sample was investigated using reflection and transmission method. Raman spectra were collected using Horiba HR Evolution-type micro-confocal laser Raman spectrometer, which ranged from 0 to 4000 cm^{-1}. Laser source was 532 nm and there were 3 acquisition cycles. Standard gemological and spectroscopy analyses were performed at the Gemmological Research Laboratory of the China University of Geosciences (Beijing). When the infrared spectroscopy and Raman spectroscopy test was performed, each sample was tested perpendicular and parallel to C-axis, except NA, which cannot be oriented.

EMPA analyses were performed at the Key Laboratory of Submarine Geosciences, State Oceanic Administration, Second Institute of Oceanography, Ministry of Natural Resources

using four-spectrometer Jeol JXA 8100 electron probe microanalyzer. Accelerating voltage was 15 kV, beam current was 20 nA, and spot size was 5 μm. The standards used were as follows: plagioclase (Al), diopside (Si, Ca), rutile (Ti), rhodonite (Mn), chromite (Fe), albite (Na), olivine (Mg), sanidine (K), apatite (P), pentlandite (Ni), and willemite (Zn). ZAF correction scheme was used for correction.

LA-ICP-MS analyses were performed at the Mineral Laser Microprobe Analysis Laboratory, China University of Geoscience (Beijing). The laser ablation system was NewWave193 UC and quadruple rod mass spectrometer was Agilent 7900. Helium was used as carrier gas in ablation system. Spot size was 50 μm, repetition rate was 6 Hz, and ablation time was 90 s. Multiple external standards, including NIST 610, BCR-2G, and internal standard (Al), were used for quantitative calculation. The detection limit of each element can be found in Table A4. All samples were tested in the perpendicular direction during EMPA and LA-ICP-MS analyses, except NA.

3. Results

3.1. Gemological Properties

The color of aquamarines from Xinjiang varies from blue-green to light blue. Due to the large number of fissures, it is difficult to observe the internal characteristics of the samples. The NA sample from South Africa shows a darker blue color and is more transparent than that from Xinjiang. The sample MG from Brazil is the most transparent and its color is intense blue. The refractive index values are as follows: XJ-1: 1.573–1.581, XJ-2: 1.562–1.569, MG: 1.561–1.570, NA: 1.582–1.590; the birefringence index ranges from 0.007 to 0.009. All samples show weak-to-moderate dichroism. Under the CCF, all the samples are pale blue-green. XJ-1, XJ-2, and NA are inert under ultraviolet fluorescence, while MG has a weak blue-white fluorescence at longwave. The specific gravity of the samples is as follows: XJ-1:2.64, XJ-2:2.62, MG:2.61, and NA:2.65. The results of standard gemological analyses are listed in Table 1.

Table 1. Gemological characteristics of aquamarine samples.

Sample	Color	RI	DR	Dichroism	CCF	UV	SG
XJ-1	Light blue	1.573–1.581	0.008	Weak	Pale green	Inert	2.68
XJ-2	Light blue	1.562–1.569	0.007	Weak	Pale green	Inert	2.68
MG	Medium blue	1.561–1.570	0.009	Moderate	Blue green	Weak blue-white at longwave	2.67
NA	Deep blue	1.582–1.590	0.008	Weak	Pale green	Inert	2.70

3.2. Spectral Characteristics

3.2.1. Infrared Spectrum

The reflectance spectra are shown in Figure 4a. The absorption of aquamarine is concentrated in the 400–1300 cm^{-1} range. The absorption peaks at 528 and 597 cm^{-1} are generated by Si-O bending vibration, and the weak absorption at 650 cm^{-1} is caused by Be-O symmetric stretching vibration. The peaks at 684, 748, and 812 cm^{-1} are generated by Si-O-Si symmetric stretching vibration, and the peak at 962 cm^{-1} is caused by O-Si-O symmetric stretching vibration. The peaks at 1024 and 1072 cm^{-1} are related to O-Si-O asymmetric stretching vibration, and the wide absorption peaks at 1248 cm^{-1} are related to Si-O-Si asymmetric stretching vibration [24,25].

The transmittance spectra are shown in Figure 4b. XJ-1, XJ-2, and NA have several absorptions around 2341 cm^{-1} and 2359 cm^{-1}, which are caused by the asymmetric stretching vibration of CO_2 [5]. The 3111 and 3165 cm^{-1} peaks in MG are related to the reaction between Na and H when forming NaH in a channel structure [26]. The 3229 cm^{-1} and 3231 cm^{-1} peaks in XJ-1 and XJ-2 are attributed to $[Fe_2(OH)_4]^{2+}$ ions, which are formed by the hydrolysis between Fe^{3+} and water molecules in the channel with the participation of alkali metal [26]. In addition, the peaks related to $[Fe_2(OH)_4]^{2+}$ ions of

samples perpendicular to the C-axis are more obvious than those of samples parallel to the c-axis.

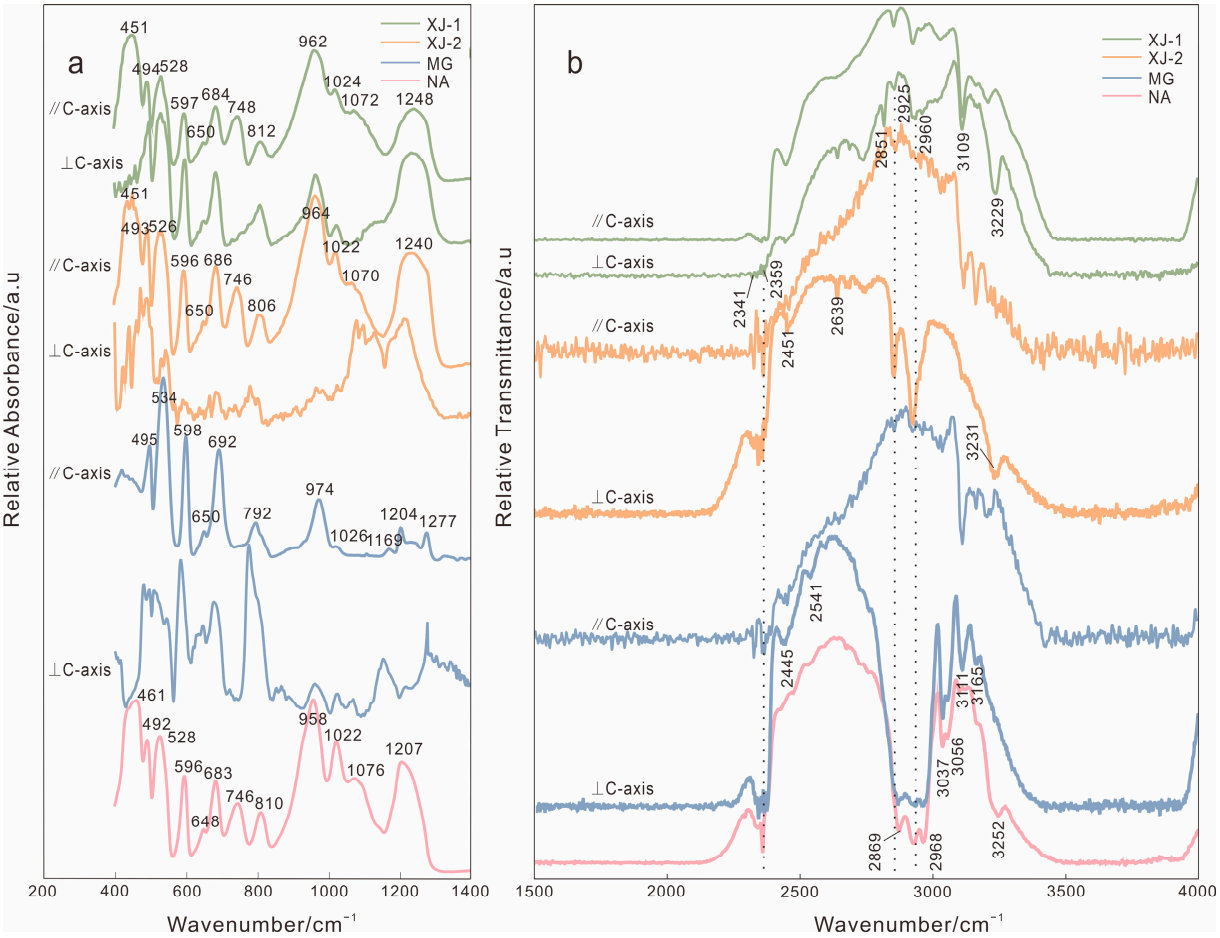

Figure 4. (**a**) Reflectance spectra of four samples. (**b**) Transmittance spectra of four samples.

The representative peaks' absorbance (or transmittance) and full width at the half maximum (FWHM) of the infrared spectrum are listed in Table A1.

3.2.2. Raman Spectrum

The spectra of the Raman spectroscopy test are shown in Figure 5. The characteristic peaks of aquamarine are concentrated at 300–1500 and 3500–3700 cm^{-1}. Two moderate peaks at 321 and 398 cm^{-1} are caused by Al-O bending vibration, and the strong peak at 686 cm^{-1} is due to Si-O-Si bending vibration. The weak peak at 1004 cm^{-1} is related to Be-O stretching vibration, and the peak at 1068 cm^{-1} is caused by Si-O stretching vibration. The peak at 1242 cm^{-1} was related to CO_2 in the channel [27].

The band in the range of 3500–3700 cm^{-1} is dominated by the vibration of water in channel. The 3608 cm^{-1} band is the absorption of type I water, which is narrow and strong, and it is not affected by alkali content. The weak 3598 cm^{-1} band is related to type II H_2O and associated with alkali content, but this band is almost undetectable [28].

It can be seen that those peaks around 1242 cm^{-1}, as well as the 3608 cm^{-1} band, have relatively higher FWHM when the aquamarine samples were tested parallel to the C-axis. This may result from CO_2 and type I water molecules being incorporated into the channel structure, they demonstrate stronger vibration when tested in parallel C-axis directions (Table A2).

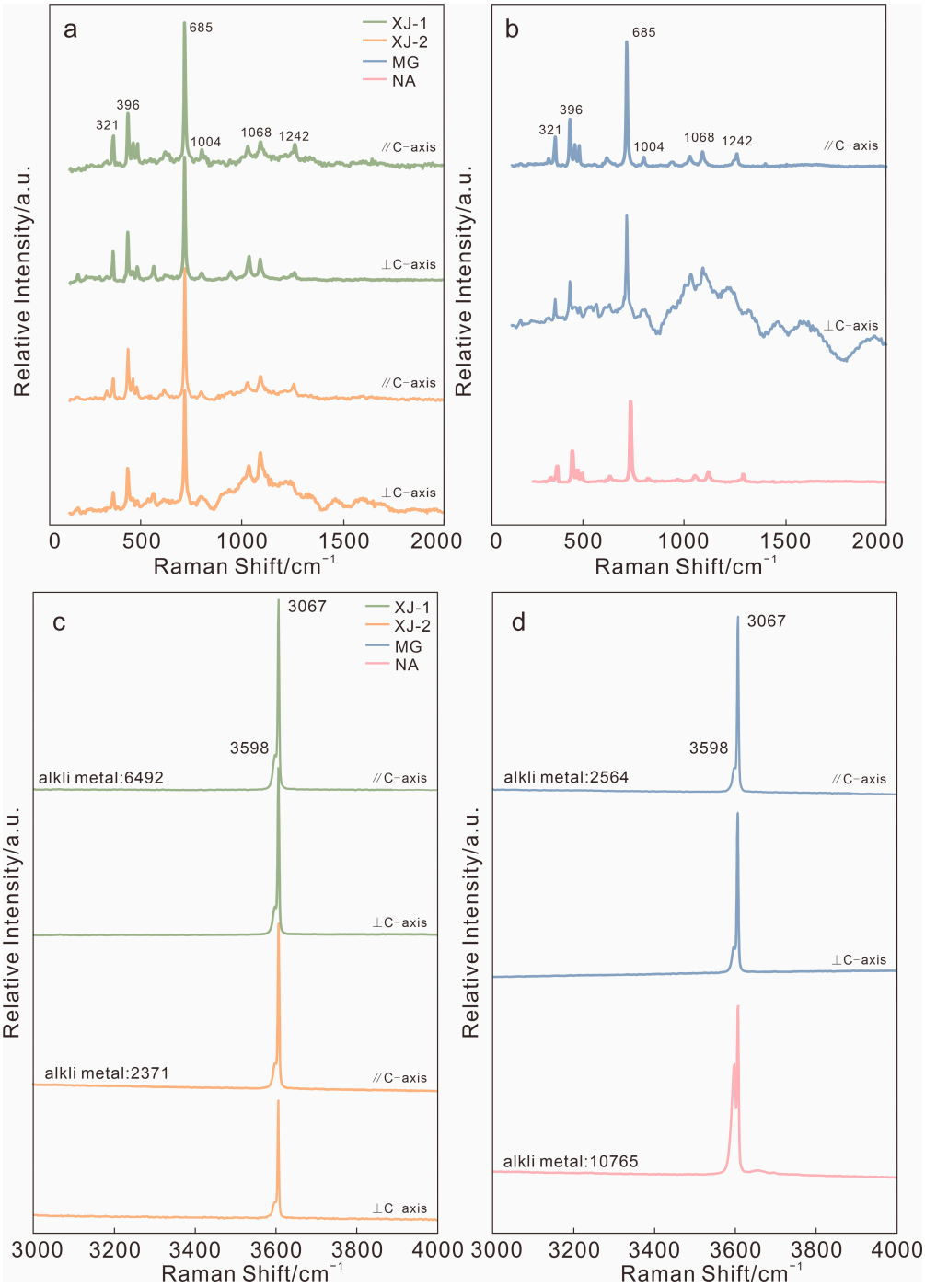

Figure 5. (**a**,**b**) Raman spectra of four aquamarine samples. (**c**,**d**) Raman spectrum related to channel water. Alkali metal content (Li, Na, K, Rb, and Cs, in ppm) analyzed using LA-ICP-MS.

3.3. Major and Trace Elements

The major element analytical results of four crystals are listed in Table A3. The major element chemical composition of the investigated aquamarine samples is mostly composed of SiO_2 (61.14–66.40 wt.%) and Al_2O_3 (17.04–20.08 wt.%), followed by chromophore element FeO (0.35–2.17 wt.%). The trace elements found include Na, Li, K, and Cs. Beryllium is also major element in aquamarine, but it cannot be detected using EMPA. Thus, EMPA data calculation based on O = 18 and Be^{2+} is assumed to be 3-Li^{+} [18]. The crystal chemical formulas of each sample are listed in Table 2 [29]. After being calculated, the sum of analysis

was still less than 100%; this may result from the amount of water in the composition of aquamarine samples.

Table 2. Ideal chemical formula of aquamarine samples.

Sample	Chemical Formula
XJ-1	$^{ch}(Na_{0.091},K_{0.002})^{T2}(Be_{2.949},Li_{0.051})_{3.000}$ $^{O}(Al_{2.117},Fe_{0.048},Mg_{0.015},Cr_{0.002},Ca_{0.001},Mn_{0.001},Ti_{0.001})_{2.185}{}^{T1}Si_{5.863}O_{18}$
XJ-2	$^{ch}(Na_{0.067},K_{0.001})^{T2}Be_{2.991},Li_{0.009})_{3.000}$ $^{O}(Al_{1.947},Fe_{0.038},Mg_{0.007},Cr_{0.001},Ca_{0.001},Mn_{0.001},Ti_{0.001})_{1.996}{}^{T1}Si_{5.999}O_{18}$
MG	$^{ch}(Na_{0.044},K_{0.001})^{T2}(Be_{2.989},Li_{0.011})_{3.000}$ $^{O}(Al_{1.890},Fe_{0.078},Mg_{0.006},Cr_{0.002},Ca_{0.001},Mn_{0.001},Ti_{0.001})_{1.979}{}^{T1}Si_{6.028}O_{18}$
NA	$^{ch}(Na_{0.234},K_{0.011})^{T2}(Be_{2.955},Li_{0.045})_{3.000}$ $^{O}(Al_{1.931},Fe_{0.166},Mg_{0.152},Mn_{0.003},Cr_{0.001},Ca_{0.001},Ti_{0.001})_{2.255}{}^{T1}Si_{5.837}O_{18}$

In beryl crystal, Al in the octahedral site can be substituted by divalent or trivalent cations, including Fe^{2+}, Fe^{3+}, Mg^{2+}, Mn^{2+}, and Cr^{3+} [3,4]. From major element composition, it can be seen that Fe is the most important substituent at the octahedral site, and ranges from 0.026 to 0.174 apfu. Na^{+} ranges from to 0.037 to 0.299 apfu, which is much higher than K^{+} (up to 0.020), Cr^{3+} (up to 0.010), Mn^{2+} (up to 0.008), Ca^{2+} (up to 0.007), Ti^{+} (up to 0.007), and Ni^{+} (up to 0.004). Na^{+} typically occupies the channel site to balance the charge difference through isomorphous substitution. NA has relatively high Fe (0.147 to 0.174), Na (0.209 to 0.299), and Mg (0.141 to 0.157) content compared with the other three samples analyzed in this study.

Data from LA-ICP-Ms were used to determine Li^{+} and other trace elements. The results of four crystals are listed in Table A4, with calculated apfu values based on assuming Si = 6 (data obtained from EMPA) [2]. Consistent with the EMPA results, Li^{+} (0.008 to 0.060) and Fe (0.040 to 0.169) are major substituents at the tetrahedral and octahedral sites, respectively. Na^{+} ranges from to 0.039 to 0.227 apfu, compare to minor Cs^{+} (up to 0.017), Sc^{3+} (<0.007), Rb^{+} (<0.001), V^{3+} (<0.001). NA was characterized by a relatively high Sc (from 537.2 to 574.2 ppm) and V (from 61 to 66 ppm) content compared with the other three samples.

Total alkali metal contents (Li^{+}, Na^{+}, K^{+}, Rb^{+}, and Cs^{+}) in aquamarine samples were calculated as seen in Figures 3d and 5c. NA has the highest alkali content of the four samples, followed by XJ-1. The alkali contents in XJ-2 and MG were similar.

4. Discussion

4.1. Gemological Properties

The standard gemological investigation showed that the color of aquamarines of different origin investigated in this work varies from almost colorless to light-greenish-blue to dark blue. It did not show significant distinction in refractive index or specific gravity. This suggests that when aquamarines show similar properties, standard gemological tests alone are not sufficient to distinguish their origin.

4.2. Spectroscopy Analysis

In the infrared spectrum (Figure 4), the band around 1020 cm^{-1} tended to become broad and strong with the increase in substitution at the octahedral site [25]. NA has the strongest band in 1020 cm^{-1}, while XJ-1 and XJ-2 are weaker. This denotes that octahedral substitution in NA is higher than aquamarine from Xinjiang. Each sample show vibrations around 700 cm^{-1} and 1070 cm^{-1}, indicating that all samples have substitution of Be^{2+} by Li^{+} at the tetrahedral site [25,30]. In addition, the absorption peaks around 746 cm^{-1} are absent when the samples are perpendicular to the C-axis (XJ-1 and XJ-2). In the spectrum of samples perpendicular to the C-axis, the absorption peak around 1200 cm^{-1} is the strongest, while the strongest peak in samples parallel to C-axis is around 964 cm^{-1} (Table A1).

In the Raman spectroscopy test, the intensities at 3607 cm^{-1} in different samples are almost the same, and NA shows the strongest absorption at 3598 cm^{-1} due to type II water,

indicating that its alkali content is the highest out of the four samples. The result of FWHM at 3598 cm^{-1} absorption is also in good agreement with alkali content. The FWHM value of NA was highest, while XJ-2 and MG were lower (Figure 5c,d).

Above all, in the spectroscopy tests, the aquamarines from three origins show distinctions mostly related to their chemical composition. It can be inferred that through the analysis of major and trace element contents of aquamarine, we can verify the conclusions obtained through the spectroscopy test and further distinguish the aquamarines from different regions.

4.3. Chemical Compositions

Figure 6 shows the negative correlation of divalent/trivalent cations with Al content based on the EMPA value of four aquamarine samples in comparison with the ideal correlation line of Al = 2 apfu to total substituent = 1 apfu. The points of XJ-2 and MG are distributed almost along the ideal correlation line, while that the fact that those of XJ-1 are offset to the right of the ideal line is probably due to high Al EMPA values, and NA's points lying above the expect trend may result from Fe^{2+} being present as Fe^{3+}.

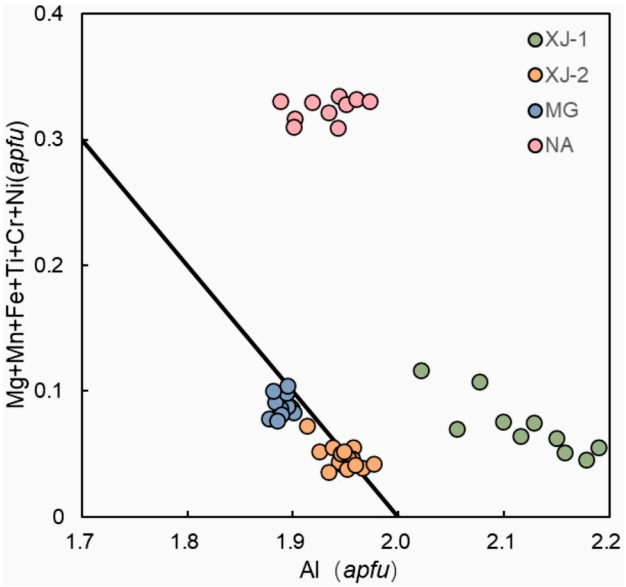

Figure 6. Plot of major octahedral ion (Al) versus its substituent in aquamarine samples. Ideal correlation line defined by Al = 2 apfu; total substituent = 1 apfu.

NA has a relatively high Sc content among the four samples (up to 500 ppm); a comparative analysis of the ratios of the content of Sc and Fe in the aquamarine samples has shown a tendency towards their positive correlation (Figure 7). Borzenko and Yurgenson [31] carried out a comparative study of the content of Sc in variously colored beryl crystals of the Sherlovogorsk ore deposit, and the maximum concentrations of Sc typical for aquamarine samples were revealed. They concluded that Sc content may be connected with Fe^{3+} content.

The alkali element contents obtained by LA-ICP-MS are plotted in Figure 8. The relative concentrations of each alkali element showed similar variation in all samples. This tendency may result from the fact that when the charge deficiency initiated by Li^{+} substitutes Be^{2+}, it is compensated by a proportional amount of Na^{+} and Cs^{+} and a minor amount of K^{+} and Rb^{+} [20]. NA has the highest alkali content, which is consistent with the conclusion obtained through the Raman spectrum.

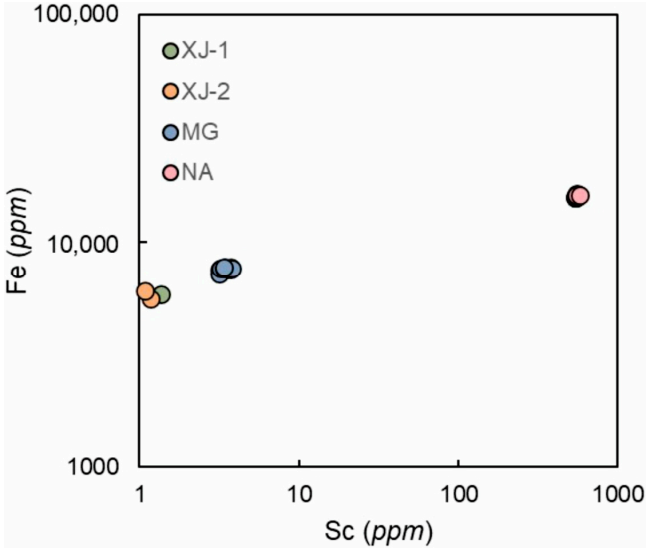

Figure 7. Plot of Sc vs. Fe content in aquamarine samples. Positive correlation between scandium and iron can be found in each sample.

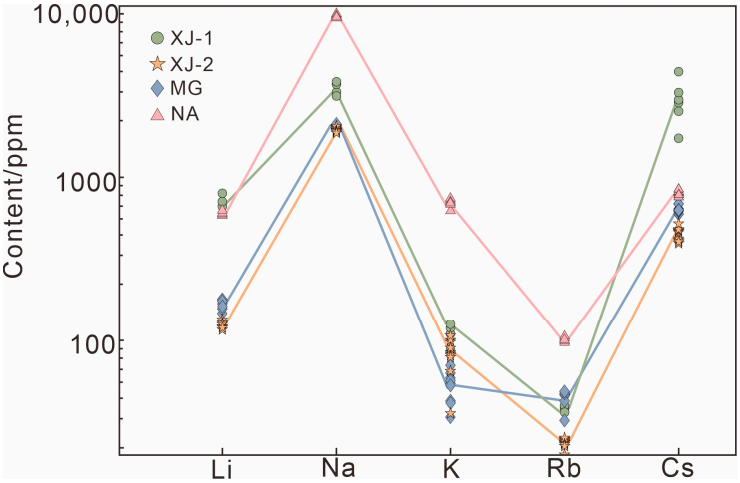

Figure 8. Alkali metal content in aquamarines have similar tendencies.

Figure 9a shows that the positive correlation of Na^+ and Li^+ is consistent with Na^+ being predominant in charge balancing, as Li^+ substitutes Be^{2+}. Those points offset upward from the line suggest that the remaining Na^+ is used for charge balance, substituting Al^{3+} with divalent cations. Figure 9b plots other alkalis vs. divalent cations at the octahedral site (excluding Fe^{2+}). The great deviation of NA data suggests that K^+, Rb^+, and Cs^+ are insufficient to balance the charge deficiency which arises from the substitution of divalent cations, so extra Na^+ is needed; this is consistent with Figure 9a. The datapoints of XJ-2 and MG are slightly offset, but the data of the XJ-1 plots follow the line. This indicates a certain number of other divalent cations present in XJ-1 (e.g., Fe^{2+}).

In Figure 9c, we assumed that Fe_{tot} was present as Fe^{2+}, and it combined both substitutions of the Li^+ for Be^{2+} at the tetrahedral site and the sum of all divalent cations that replaced Al^{3+} at the octahedral site. It can be seen that the data of each sample have a right lateral offset to the expected trend. This suggest that divalent cations may be overestimated, and some Fe cations should present as Fe^{3+}. If we assumed Fe_{tot} present as Fe^{3+} (Figure 9d), NA still has a great deviation from the correlation line, followed by XJ-2 and MG. XJ-1 shows less deviation in both Figure 9c,d.

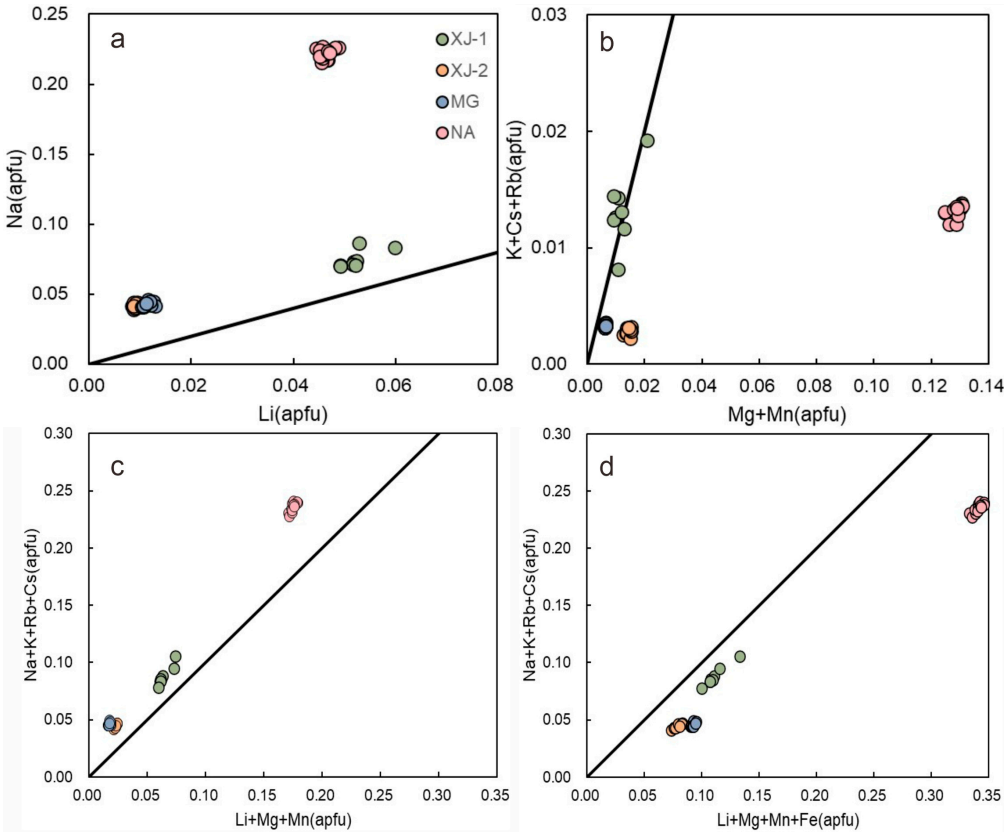

Figure 9. Correlations and trends in major and trace element variations (base on LA-ICP-MS data). (**a**) Correlation between Li^+ substitution of Be^{2+} with Na^+ charge balancing at the channel site. (**b**) Monovalent (excluding Na^+) vs. divalent cations which substitute Al^{3+} (excluding Fe^{2+}). (**c**,**d**) Combined tetrahedral and octahedral substitution expressed as alkali cations vs. Li^++ divalent cations. Black lines represent the ideal substitution or charge balance relationship, (**a**) $Li^+ = Na^+$; (**b**) $R^+ - Na^+ = X^{2+}$; (**c**) $R^+ = Li^+ + X^{2+} - Fe^{3+}$; (**d**) $R^+ = Li^+ + X^{2+}$.

The color mechanism of aquamarine is not well understood. One suggestion for bluetone in beryl is that it is the result of different Fe^{2+}/Fe^{3+} ratios [3,32,33]. Viana et al. [34] proposed that the color of beryl is dictated by the relative proportions of both Fe^{3+} at the octahedral site and Fe^{2+} at the channel site, and demonstrated that deep blue beryls have little Fe^{3+}. Another suggestion is that the intervalence charge transfer (IVTC) occurs between Fe^{2+} and Fe^{3+}, whereby the Fe^{2+} is located at the octahedral site and the Fe^{3+} is located at an interstitial octahedral position [35,36].

Owing to the absence of exact Fe^{2+}/Fe^{3+} analyses, we assumed that all Fe^{2+}/Fe^{3+} ions occupy the octahedral site. The combined results of Figure 9c,d can be summarized as follows: NA has highest Fe^{3+} content among the four samples, followed by XJ-2, which is closed to MG. XJ-1 may has lowest content of Fe^{3+} (NA > XJ-2 ≈ MG > XJ-1). Due to the complex substitutions in beryl, further experimental work would be necessary to interpret the relationship of Fe^{2+}/Fe^{3+} ions accurately.

4.4. Chemical Composition Comparison with Other Localities

Figure 10a shows the content of the major octahedral site ion (Al) and its principal substituent (Fe) in aquamarines of different origin. Comparing aquamarine samples from the literature, the Yukon Territory, Canada aquamarine is easy to distinguish due to its high Fe content, while other producing areas and the four aquamarine samples investigated in this paper are characterized by a relatively high Al content. Aquamarine from Ghorveh, Iran and Xinjiang, China may have higher Al contents than those of other origins.

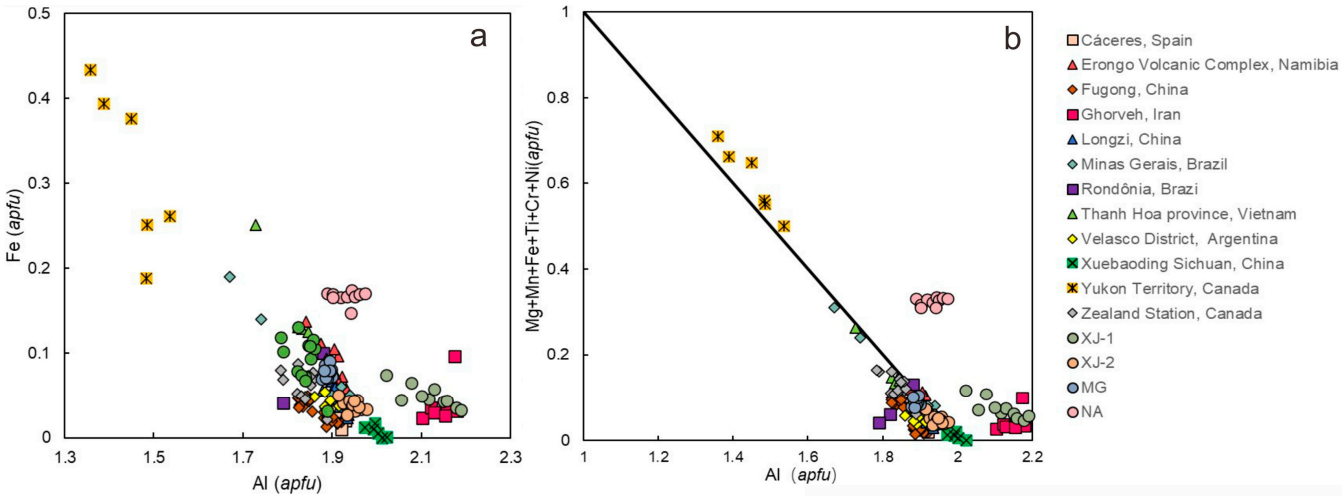

Figure 10. (**a**) Plot of Al versus Fe (apfu) in aquamarines from across the globe, showing the negative relationship between them. (**b**) Al versus substituent at the octahedral site (apfu) in aquamarines from across the globe. Ideal correlation line: Al = 2 apfu to total substituent = 1 apfu. Data from [1,2,7,9,29,34,36–41].

A negative relationship between Al and other mutual substituents at the octahedral site is observed in Figure 10b. In most cases, the substitutional trends in worldwide samples are comparable to the theoretical correlation line. XJ-1, NA, and aquamarines from Canada and Iran are plotted above the ideal correlation line. The high value of substituents at the octahedral site is characteristic of Canadian aquamarines. XJ-1, XJ-2, and MG have a low number of octahedral substituents, while NA has slightly more octahedral substituents than aquamarines from other provenances.

A negative correlation between the content of Sc versus Fe in aquamarines of different origin can be seen in Figure 11, in which two clusters of data emerge.

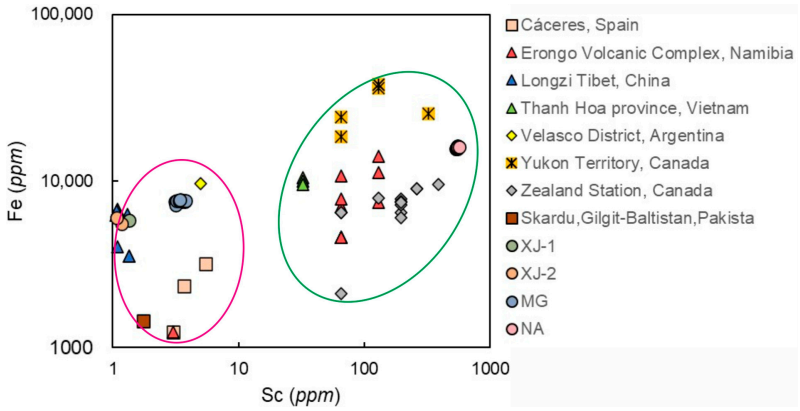

Figure 11. Sc versus Fe content in beryls from across the globe. Data from [7,28,29,36,37,40–42].

An Fe content up to 42,000 ppm and Sc up to 570 ppm are characteristic of the first group, while Fe content up to 9700 ppm and Sc from 1 to 7 ppm are typical for the second group. The first group includes aquamarines from Canada, Namibia, and Vietnam, and the second consists of aquamarines from Spain, Pakistan, Argentina, and China. The points of XJ-1, XJ-2, and MG lie in the second group, while the points of NA in first group are characterized by relatively high Sc content.

According to Hu and Lu [20], beryl can be divided into the "high-alkali beryl" group and the "low-alkali beryl" group base on Li vs. Cs content (Figure 12). Beryls from most origins belong to the low-alkali group, including four samples analyzed in this study, and only a few types of aquamarine belong to the high-alkali group (Mogok, Myanmar, and

Brazil). Though alkali content cannot distinguish aquamarine origin directly, it can roughly separate types of aquamarine and provide a reference for origin determination.

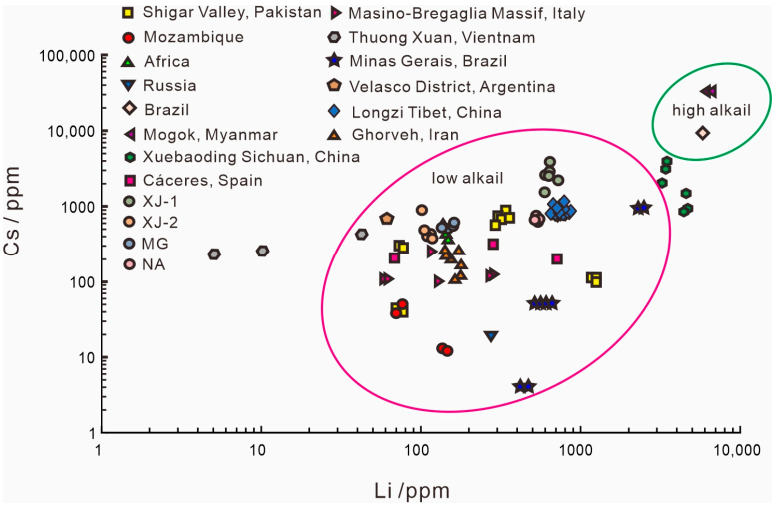

Figure 12. Li versus Cs content in beryls from across the globe. Beryls were classified as low-alkali group or high-alkali group. Data from [1,2,7,20,28,29,34,37,43].

5. Conclusions

Aquamarines from Xinjiang show weaker substitution at the octahedral site and lower alkali content than aquamarines from Namaqualand, according to spectroscopy analysis. The absorption of NaH and $[Fe_2(OH)_4]^{2+}$ ions can be found in the infrared spectrum of Minas Gerais and Xinjiang aquamarines, respectively. Raman spectroscopy revealed that Namaqualand aquamarine has the strongest type II water absorption. However, there still much overlap between the infrared and Raman spectra of aquamarines. It is thus suggested that spectroscopy analysis can be used as supplemental data during aquamarine origin determination, rather than distinguishing aquamarines' origins independently.

Major and trace element results show that octahedral substitution is predominant in aquamarines from three origins, and their alkali contents have similar proportional tendency. Comparing aquamarines from other origins, aquamarines from Xinjiang and Minas Gerais have a relatively high Al content and low Fe content, and they belong to the low-alkali group. The Namaqualand aquamarine is characterized by its high Sc content. Though verifying the certain origin of aquamarine is not easy, it is suggested that spectroscopy characteristics and major and trace elements composition should be considered comprehensively in origin identification.

Author Contributions: Writing—original draft, S.C.; writing—review and editing, S.C., B.X., J.S., Z.M. and Z.W.; investigation, S.C. and J.S.; data curation, S.C. and J.S.; software, S.C. and J.S.; methodology, B.X.; resources, B.X. All authors have read and agreed to the published version of the manuscript.

Funding: This research was funded by the National Natural Science Foundation of China (42222304, 42073038), the "Deep-time Digital Earth" Science and Technology Leading Talents Team Funds for the Central Universities for the Frontiers Science Center for Deep-time Digital Earth, China University of Geosciences (Beijing) (Fundamental Research Funds for the Central Universities; grant number: 2652023001 and 265QZ2021012), and IGCP-662.

Data Availability Statement: The data presented in this study are available within the article.

Acknowledgments: We sincerely thank the editor and anonymous reviewers for their constructive comments, which greatly contributed to enhancing the quality of our paper. This is the 20th contribution of B.X. for the National Mineral Rock and Fossil Specimens Resource Center.

Conflicts of Interest: The authors declare no conflict of interest.

Appendix A

Table A1. Representative peaks' absorbance (or transmittance) and FWHM of infrared spectrum.

	XJ-1//C		XJ-1⊥C		XJ-2//C		XJ-2⊥C		BX//C		BX⊥C		NF	
Peak (cm^{-1})	**Absorbance**	**FWHM**	**Absorbance**	**FWHM**	**Absorbance**	**FWHM**	**Absorbance**	**FWHM**	**Absorbance**	**FWHM**	**Absorbance**	**FWHM**	**Absorbance**	**FWHM**
684	0.2805	0.134	0.1632	0.122	0.0365	0.156	0.2789	0.016	0.1566	0.117	0.2518	0.116	0.3220	0.184
748	0.2453	0.140	0.0398	0.001	0.0225	0.128	0.2238	0.005	0.0327	0.038	0.0795	0.299	0.2450	0.130
962	0.4830	0.223	0.1578	0.126	0.0400	0.226	0.4628	0.009	0.0925	0.063	0.1221	0.050	0.6021	0.336
1024	0.3338	0.037	0.0599	0.030	0.0400	0.050	0.3163	0.007	0.0317	0.004	0.0861	0.033	0.4552	0.136
1072	0.2651	0.040	0.0247	0.002	0.0726	0.024	0.2341	0.015	0.0212	0.001	0.0528	0.023	0.3304	0.049
1248	0.2694	0.206	0.2000	0.154	0.0649	0.252	0.3131	0.040	0.0566	0.026	0.2862	0.128	0.3872	0.287
3231	0.0633	0.006	0.0122	0.007	0.0022	0.001	0.0152	0.005						

FWHM = full width at half maximum.

Table A2. Representative peaks' absorbance and FWHM of Raman spectrum.

	XJ-1//C		XJ-1⊥C		XJ-2//C		XJ-2⊥C		BX//C		BX⊥C		NF	
Shift (cm^{-1})	**Intensity**	**FWHM**	**Intensity**	**FWHM**	**Intensity**	**FWHM**	**Intensity**	**FWHM**	**Intensity**	**FWHM**	**Intensity**	**FWHM**	**Intensity**	**FWHM**
1243	174.872	88.516	114.567	66.595	230.673	70.238	382.072	69.447	184.364	194.734	1161.451	85.750	226.127	4.052
3598	1769.940	66.976	1486.210	99.910	2749.440	146.693	945.105	35.649	850.065	49.907	1678.470	39.167	2607.280	919.442
3609	7288.890	5795.524	5365.190	4085.822	8139.720	5725.512	5679.880	1739.932	5905.450	3257.087	5677.110	1524.773	3781.540	1479.543

FWHM = full width at half maximum.

Table A3. EMPA analyses of aquamarine samples (wt.%).

	XJ-1-1	XJ-1-2	XJ-1-3	XJ-1-4	XJ-1-5	XJ-1-6	XJ-1-7	XJ-1-8	XJ-1-9	XJ-1-10	XJ-2-1	XJ-2-2	XJ-2-3	XJ-2-4	XJ-2-5	XJ-2-6
SiO_2	63.19	63.77	63.52	62.87	62.65	63.26	62.81	63.07	62.64	62.92	65.76	65.88	65.76	66.40	65.96	65.71
Na_2O	0.49	0.61	0.43	0.48	0.64	0.46	0.45	0.47	0.53	0.46	0.46	0.42	0.39	0.34	0.35	0.33
K_2O	0.03	0.03	0.01	0.03	0.04	0.02	0.02	0.00	0.02	bdl	0.03	0.01	0.02	0.01	0.01	0.00
Cr_2O_3	bdl	0.05	bdl	bdl	0.04	0.04	0.01	bdl	0.03	0.06	bdl	0.03	0.01	bdl	0.03	bdl
Al_2O_3	18.65	18.51	19.42	19.39	18.80	19.19	19.60	19.75	19.87	20.08	17.87	18.05	18.24	18.39	18.16	18.15
MgO	0.17	0.24	0.04	0.11	0.26	0.10	0.05	0.02	0.04	0.08	0.08	0.06	0.03	0.05	0.04	0.01
CaO	0.01	0.02	0.01	0.00	0.00	0.02	0.02	0.01	0.02	bdl	0.00	0.01	0.01	0.07	0.01	bdl
MnO	bdl	0.06	bdl	bdl	0.04	0.00	0.01	0.05	bdl	0.03	bdl	bdl	0.07	0.01	bdl	0.02
P_2O_5	0.04	bdl	0.02	bdl	0.00	0.05	bdl	bdl	0.03	bdl	bdl	0.01	0.03	0.01	bdl	0.01
FeO	0.57	0.95	0.58	0.73	0.82	0.63	0.55	0.56	0.45	0.41	0.53	0.57	0.59	0.48	0.45	0.50
TiO_2	bdl	bdl	bdl	bdl	bdl	bdl	0.09	0.01	bdl	bdl	bdl	0.03	0.01	0.04	0.01	0.02
NiO	0.04	0.04	0.18	0.03	0.03	0.13	0.07	bdl	0.04	0.10	bdl	bdl	bdl	0.01	bdl	0.05
Li_2O	0.14	0.14	0.14	0.14	0.16	0.13	0.14	0.13	0.13	0.13	0.02	0.02	0.02	0.02	0.02	0.03
BeO *	13.13	13.25	13.28	13.18	13.07	13.24	13.19	13.26	13.20	13.27	13.62	13.67	13.68	13.80	13.68	13.64
Total	96.44	97.66	97.62	96.95	96.54	97.27	97.00	97.32	96.99	97.53	98.38	98.75	98.85	99.62	98.73	98.47
cation (apfu)																
Si	5.909	5.908	5.872	5.857	5.872	5.872	5.845	5.847	5.827	5.821	6.011	6.000	5.986	5.992	6.003	5.998
Na	0.089	0.110	0.076	0.086	0.116	0.083	0.082	0.085	0.096	0.082	0.082	0.074	0.068	0.060	0.062	0.058
K	0.003	0.003	0.002	0.003	0.005	0.002	0.002	0.000	0.002	0.000	0.003	0.001	0.002	0.001	0.002	0.000
Cr	0.000	0.003	0.000	0.000	0.003	0.003	0.000	0.000	0.002	0.004	0.000	0.002	0.001	0.000	0.002	0.000
Al	2.055	2.021	2.115	2.128	2.077	2.100	2.149	2.157	2.178	2.189	1.925	1.938	1.957	1.956	1.948	1.952
Mg	0.023	0.033	0.006	0.016	0.036	0.014	0.007	0.003	0.006	0.011	0.011	0.008	0.004	0.007	0.005	0.002
Ca	0.001	0.002	0.001	0.000	0.000	0.002	0.002	0.000	0.002	0.000	0.000	0.001	0.001	0.007	0.001	0.000
Mn	0.000	0.004	0.000	0.000	0.003	0.000	0.001	0.004	0.000	0.002	0.000	0.000	0.005	0.000	0.000	0.002

Table A3. *Cont.*

P	0.003	0.000	0.001	0.000	0.000	0.004	0.000	0.000	0.002	0.000	0.000	0.001	0.002	0.001	0.000	0.001
Fe	0.044	0.074	0.045	0.057	0.065	0.049	0.043	0.043	0.035	0.032	0.041	0.044	0.045	0.036	0.034	0.038
Ti	0.000	0.000	0.000	0.000	0.000	0.000	0.007	0.001	0.000	0.000	0.000	0.002	0.000	0.002	0.000	0.002
Ni	0.003	0.003	0.014	0.002	0.002	0.010	0.005	0.000	0.003	0.007	0.000	0.000	0.000	0.001	0.000	0.004
Li	0.051	0.051	0.050	0.051	0.058	0.048	0.051	0.048	0.050	0.050	0.009	0.008	0.008	0.009	0.009	0.009
Be	2.949	2.949	2.950	2.949	2.942	2.952	2.949	2.952	2.950	2.950	2.991	2.992	2.992	2.991	2.991	2.991
	XJ-2-7	**XJ-2-8**	**XJ-2-9**	**XJ-2-10**	**XJ-2-11**	**XJ-2-12**	**XJ-2-13**	**XJ-2-14**	**XJ-2-15**	**MG-1**	**MG-2**	**MG-3**	**MG-4**	**MG-5**	**MG-6**	**MG-7**
SiO_2	65.82	65.42	65.81	64.99	66.00	66.06	65.34	65.97	65.58	65.48	65.09	65.37	65.73	65.43	64.97	65.36
Na_2O	0.37	0.38	0.36	0.44	0.37	0.38	0.30	0.36	0.39	0.23	0.25	0.21	0.24	0.21	0.23	0.24
K_2O	0.00	0.01	0.02	0.01	0.01	0.01	0.01	bdl	0.01	bdl	0.02	0.01	0.00	0.01	0.01	0.00
Cr_2O_3	0.01	bdl	bdl	bdl	0.04	bdl	0.02	bdl	bdl	0.01	bdl	0.01	bdl	bdl	0.06	bdl
Al_2O_3	18.32	17.97	18.16	17.56	18.16	18.02	18.31	18.29	18.08	17.48	17.41	17.22	17.47	17.51	17.33	17.35
MgO	0.04	0.04	0.03	0.14	0.04	0.05	0.04	0.04	0.06	0.01	0.04	0.04	0.07	0.05	0.03	0.06
CaO	0.01	bdl	0.01	bdl	0.02	0.00	bdl	0.01	0.02	bdl	0.01	0.01	0.01	0.00	0.00	bdl
MnO	bdl	0.03	0.01	bdl	0.03	bdl	0.02	0.01	0.00	0.04	bdl	0.03	0.01	0.01	bdl	bdl
P_2O_5	bdl	0.03	0.01	0.00	bdl	0.02	bdl	0.01	0.00	bdl	0.02	bdl	0.01	0.01	0.01	0.01
FeO	0.43	0.47	0.41	0.64	0.50	0.35	0.44	0.47	0.57	1.02	1.04	0.90	1.02	0.94	1.00	1.02
TiO_2	bdl	bdl	0.03	0.04	bdl	0.04	0.02	bdl	0.01	bdl	0.01	0.00	0.01	0.02	0.02	bdl
NiO	bdl	bdl	bdl	0.03	0.01	bdl	bdl	bdl	0.01	0.06	0.01	bdl	bdl	0.02	0.01	bdl
Li_2O	0.02	0.02	0.02	0.02	0.02	0.03	0.02	0.02	0.02	0.03	0.03	0.03	0.03	0.03	0.03	0.03
BeO *	13.68	13.57	13.66	13.46	13.70	13.68	13.60	13.70	13.62	13.52	13.45	13.45	13.57	13.51	13.41	13.48
Total	98.72	97.94	98.52	97.34	98.91	98.63	98.13	98.87	98.35	97.89	97.36	97.28	98.17	97.76	97.11	97.55

Table A3. *Cont.*

cation (apfu)																
Si	5.991	6.003	6.001	6.009	6.000	6.014	5.984	5.996	5.996	6.026	6.022	6.046	6.029	6.025	6.025	6.033
Na	0.066	0.068	0.064	0.079	0.066	0.068	0.054	0.063	0.069	0.041	0.044	0.037	0.043	0.038	0.041	0.043
K	0.000	0.002	0.002	0.001	0.002	0.002	0.001	0.000	0.001	0.000	0.002	0.001	0.000	0.002	0.001	0.000
Cr	0.001	0.000	0.000	0.000	0.003	0.000	0.001	0.000	0.000	0.001	0.000	0.001	0.000	0.000	0.004	0.000
Al	1.965	1.943	1.951	1.914	1.945	1.933	1.976	1.959	1.948	1.896	1.898	1.877	1.889	1.900	1.894	1.887
Mg	0.006	0.006	0.005	0.019	0.006	0.007	0.005	0.005	0.008	0.002	0.005	0.006	0.010	0.007	0.004	0.008
Ca	0.001	0.000	0.001	0.000	0.002	0.000	0.000	0.000	0.001	0.000	0.001	0.001	0.001	0.000	0.000	0.000
Mn	0.000	0.002	0.000	0.000	0.002	0.000	0.001	0.001	0.000	0.003	0.000	0.002	0.001	0.000	0.000	0.000
P	0.000	0.002	0.001	0.000	0.000	0.001	0.000	0.001	0.000	0.000	0.001	0.000	0.001	0.000	0.000	0.001
Fe	0.033	0.036	0.031	0.049	0.038	0.026	0.033	0.036	0.043	0.078	0.081	0.069	0.078	0.072	0.078	0.079
Ti	0.000	0.000	0.002	0.003	0.000	0.003	0.002	0.000	0.000	0.000	0.001	0.000	0.000	0.002	0.002	0.000
Ni	0.000	0.000	0.000	0.002	0.001	0.000	0.000	0.000	0.000	0.004	0.000	0.000	0.000	0.002	0.001	0.000
Li	0.009	0.009	0.009	0.010	0.009	0.009	0.009	0.009	0.009	0.011	0.011	0.013	0.011	0.012	0.013	0.012
Be	2.991	2.991	2.991	2.990	2.991	2.991	2.991	2.991	2.991	2.989	2.989	2.987	2.989	2.988	2.987	2.988
	MG-8	**MG-9**	**MG-10**	**MG-11**	**MG-12**	**MG-13**	**NA-1**	**NA-2**	**NA-3**	**NA-4**	**NA-5**	**NA-6**	**NA-7**	**NA-8**	**NA-9**	**NA-10**
SiO_2	65.33	65.29	65.58	65.44	64.58	65.56	62.51	62.64	61.65	61.54	61.54	61.96	61.55	62.50	61.14	61.59
Na_2O	0.21	0.25	0.27	0.26	0.31	0.27	1.27	1.16	1.30	1.63	1.30	1.30	1.31	1.16	1.15	1.23
K_2O	0.01	0.01	0.01	bdl	0.01	0.01	0.08	0.09	0.09	0.17	0.07	0.08	0.09	0.05	0.12	0.08
Cr_2O_3	bdl	0.02	bdl	0.02	0.13	0.11	bdl	0.01	0.00	bdl	bdl	bdl	0.01	0.05	0.01	bdl
Al_2O_3	17.30	17.34	17.38	17.47	17.28	17.37	17.07	17.21	17.17	17.36	17.42	17.04	17.50	17.63	17.49	17.76
MgO	0.03	0.01	0.02	0.02	0.10	0.05	1.09	1.04	1.09	1.07	1.11	1.00	1.09	1.12	1.09	1.10
CaO	0.01	bdl	bdl	0.00	0.08	bdl	0.00	bdl	0.00	0.02	0.01	0.01	bdl	0.02	0.03	0.01
MnO	0.02	0.04	0.02	0.02	0.01	bdl	0.04	0.01	0.04	0.03	0.02	0.03	0.09	0.01	0.05	0.07

Table A3. *Cont.*

P_2O_5	0.01	bdl	bdl	0.01	bdl	bdl	0.01	bdl	bdl	0.04	bdl	0.02	0.01	0.02	bdl	0.03
FeO	1.11	0.91	0.92	1.17	1.02	1.04	2.17	2.16	2.09	2.11	2.20	2.10	2.11	1.88	2.13	2.16
TiO_2	bdl	0.03	0.00	0.02	bdl	0.05	0.05	0.00	bdl	bdl	0.01	0.01	bdl	0.01	0.01	bdl
NiO	bdl	0.03	0.01	0.01	0.00	0.04	0.02	0.00	0.09	0.04	0.02	bdl	bdl	0.01	0.05	0.00
Li_2O	0.03	0.03	0.03	0.03	0.03	0.03	0.12	0.12	0.12	0.12	0.12	0.12	0.11	0.12	0.12	0.12
BeO *	13.47	13.47	13.52	13.53	13.37	13.54	13.10	13.12	12.98	13.02	12.99	13.00	13.02	13.16	12.93	13.04
Total	97.52	97.43	97.76	98.00	96.93	98.06	97.54	97.57	96.62	97.14	96.81	96.67	96.89	97.74	96.30	97.20
cation (apfu)																
Si	6.034	6.033	6.038	6.019	6.009	6.025	5.867	5.872	5.845	5.816	5.824	5.865	5.820	5.842	5.816	5.805
Na	0.037	0.044	0.048	0.045	0.056	0.048	0.232	0.210	0.239	0.299	0.238	0.239	0.240	0.209	0.213	0.224
K	0.001	0.001	0.001	0.000	0.001	0.001	0.010	0.010	0.011	0.020	0.009	0.010	0.011	0.006	0.015	0.010
Cr	0.000	0.002	0.000	0.002	0.010	0.008	0.000	0.001	0.000	0.000	0.000	0.000	0.001	0.004	0.001	0.000
Al	1.883	1.889	1.885	1.894	1.895	1.881	1.888	1.901	1.918	1.933	1.943	1.901	1.951	1.942	1.960	1.973
Mg	0.004	0.002	0.003	0.003	0.014	0.006	0.153	0.145	0.154	0.150	0.157	0.141	0.154	0.156	0.155	0.155
Ca	0.001	0.000	0.000	0.000	0.007	0.000	0.000	0.000	0.000	0.002	0.001	0.001	0.000	0.002	0.003	0.001
Mn	0.001	0.003	0.002	0.002	0.001	0.000	0.003	0.001	0.003	0.002	0.002	0.003	0.008	0.001	0.004	0.005
P	0.001	0.000	0.000	0.001	0.000	0.000	0.001	0.000	0.000	0.003	0.000	0.002	0.001	0.002	0.000	0.002
Fe	0.086	0.070	0.071	0.090	0.080	0.080	0.170	0.169	0.166	0.166	0.174	0.166	0.167	0.147	0.169	0.170
Ti	0.000	0.002	0.000	0.001	0.000	0.004	0.003	0.000	0.000	0.000	0.001	0.000	0.000	0.001	0.001	0.000
Ni	0.000	0.002	0.000	0.001	0.000	0.003	0.002	0.000	0.007	0.003	0.002	0.000	0.000	0.001	0.004	0.000
Li	0.012	0.011	0.010	0.011	0.012	0.011	0.046	0.045	0.044	0.044	0.047	0.045	0.043	0.045	0.044	0.047
Be	2.988	2.989	2.990	2.989	2.988	2.989	2.954	2.955	2.956	2.956	2.953	2.955	2.957	2.955	2.956	2.953

* = calculated on the basis of O = 18, Be = 3-Li. Li_2O recalculated from LA-ICP-MS data. bdl = below detection limit.

Table A4. LA-ICP-MS analyses of aquamarine samples (ppm).

	XJ-1-1	XJ-1-2	XJ-1-3	XJ-1-4	XJ-1-5	XJ-1-6	XJ-1-7	XJ-1-8	XJ-2-1	XJ-2-2	XJ-2-3	XJ-2-4	XJ-2-5	XJ-2-6	XJ-2-7	XJ-2-8	XJ-2-9
Li	630	641	630	631	721	598	639	596	112	106	108	113	112	117	114	112	110
Na	2948	3002	2890	2840	3327	2851	3470	2807	1768	1738	1770	1742	1634	1689	1688	1680	1815
Mg	407	440	380	378	523	492	869	441	612	582	609	590	536	580	578	580	646
K	78.9	90.7	77.5	97.8	107	90.8	113.1	84.3	90.1	87.5	71.2	75.2	67.7	96.0	70.8	74.5	81.7
Sc	bdl	0.43	0.28	bdl	0.30	0.57	1.36	0.31	0.93	0.96	0.70	0.89	0.69	0.87	0.77	0.92	0.87
Ti	79.2	71.2	71.8	66.7	63.1	70.6	73.9	68.7	67.7	61.3	66.9	64.2	63.5	66.3	69.5	70.1	70.1
V	2.27	2.51	2.16	2.25	2.26	2.48	8.01	1.32	1.45	1.42	1.39	1.44	1.11	1.44	1.22	1.29	1.53
Mn	36.6	36.6	35.9	35.8	32.3	37.0	44.3	28.8	73.9	70.9	68.4	70.3	62.2	61.1	58.9	65.6	72.2
Fe	4492	4751	4550	4655	4159	4535	5782	3907	5805	5774	5723	5698	5293	5388	5401	5472	5985
Zn	371	370	360	375	346	373	356	348	201	202	199	204	201	202	201	199	202
Rb	33.3	35.9	30.3	35.7	33.3	34.4	41.4	30.4	22.5	23.1	21.8	21.7	20.7	21.6	20.2	21.6	22.4
Cs	2623	2989	2593	2969	2278	2683	4000	1562	427	424	404	412	357	378	377	366	468
cation (apfu)																	
Li	0.052	0.052	0.052	0.052	0.060	0.049	0.053	0.049	0.009	0.008	0.008	0.009	0.009	0.009	0.009	0.009	0.009
Na	0.073	0.074	0.071	0.071	0.083	0.071	0.087	0.070	0.042	0.041	0.042	0.041	0.039	0.040	0.040	0.040	0.043
Mg	0.010	0.010	0.009	0.009	0.012	0.012	0.021	0.010	0.014	0.013	0.014	0.013	0.012	0.013	0.013	0.013	0.015
K	0.001	0.001	0.001	0.001	0.002	0.001	0.002	0.001	0.001	0.001	0.001	0.001	0.001	0.001	0.001	0.001	0.001
Sc	-	0.000	0.000	-	0.000	0.000	0.000	0.000	0.000	0.000	0.000	0.000	0.000	0.000	0.000	0.000	0.000
Ti	0.001	0.001	0.001	0.001	0.001	0.001	0.001	0.001	0.001	0.001	0.001	0.001	0.001	0.001	0.001	0.001	0.001
V	0.000	0.000	0.000	0.000	0.000	0.000	0.000	0.000	0.000	0.000	0.000	0.000	0.000	0.000	0.000	0.000	0.000
Mn	0.000	0.000	0.000	0.000	0.000	0.000	0.000	0.000	0.001	0.001	0.001	0.001	0.001	0.001	0.001	0.001	0.001
Fe	0.046	0.048	0.046	0.048	0.043	0.046	0.059	0.040	0.057	0.057	0.056	0.055	0.052	0.053	0.053	0.054	0.059
Zn	0.003	0.003	0.003	0.003	0.003	0.003	0.003	0.003	0.002	0.002	0.002	0.002	0.002	0.002	0.002	0.002	0.002
Rb	0.000	0.000	0.000	0.000	0.000	0.000	0.000	0.000	0.000	0.000	0.000	0.000	0.000	0.000	0.000	0.000	0.000
Cs	0.011	0.013	0.011	0.013	0.010	0.012	0.017	0.007	0.002	0.002	0.002	0.002	0.001	0.002	0.002	0.002	0.002

Table A4. *Cont.*

	XJ-2-10	XJ-2-11	XJ-2-12	XJ-2-13	MG-1	MG-2	MG-3	MG-4	MG-5	MG-6	MG-7	MG-8	MG-9	MG-10	MG-11	MG-12	MG-13
Li	119	112	116	109	135	144	158	136	144	161	151	145	137	131	135	147	135
Na	1828	1853	1829	1732	1764.2	1778	1857	1731	1779	1728	1770	1905	1732	1723	1735	1849	1721
Mg	631	648	632	600	212	220	222	225	225	221	227	230	228	230	230	230	230
K	32.2	58.3	69.5	83.8	63	39.4	38.0	48.7	63.5	31.0	39.3	63.2	73.8	71.5	53.3	49.7	57.2
Sc	1.18	0.74	1.08	0.69	3.25	3.14	3.32	3.52	3.22	3.18	3.76	3.45	3.43	3.22	3.45	3.76	3.36
Ti	68.9	70.5	70.3	73.1	65.8	67.9	66.3	69.4	64.6	64.4	64.4	66.7	70.9	70.8	67.5	68.5	72.8
V	1.64	1.53	1.11	1.34	7.29	7.37	7.50	7.34	7.27	7.25	7.72	7.40	7.00	7.63	7.72	7.12	7.71
Mn	61.0	75.8	73.0	74.2	105	102	95.0	107	104	104	111	117	117	119	118	122	120
Fe	5529	6026	5992	5826	7546	7504	7457	7503	7547	7204	7522	7585	7575	7633	7663	7649	7634
Zn	191	206	199	207	87.6	85.3	84.9	86.0	85.1	82.1	89.7	87.0	90.5	86.0	89.2	88.1	89.1
Rb	18.2	21.2	20.9	21.9	43.5	39.1	29.7	42.5	42.2	29.1	39.1	42.1	43.3	42.6	38.7	42.1	43.2
Cs	395	465	464	431	543	555	578	543	555	621	563	556	542	546	546	559	548
cation (apfu)																	
Li	0.009	0.009	0.009	0.009	0.011	0.011	0.013	0.011	0.011	0.013	0.012	0.012	0.011	0.010	0.011	0.012	0.011
Na	0.044	0.044	0.043	0.042	0.042	0.043	0.045	0.041	0.043	0.042	0.042	0.046	0.042	0.041	0.042	0.045	0.041
Mg	0.014	0.015	0.014	0.014	0.005	0.005	0.005	0.005	0.005	0.005	0.005	0.005	0.005	0.005	0.005	0.005	0.005
K	0.000	0.001	0.001	0.001	0.001	0.001	0.001	0.001	0.001	0.000	0.001	0.001	0.001	0.001	0.001	0.001	0.001
Sc	0.000	0.000	0.000	0.000	0.000	0.000	0.000	0.000	0.000	0.000	0.000	0.000	0.000	0.000	0.000	0.000	0.000
Ti	0.001	0.001	0.001	0.001	0.001	0.001	0.001	0.001	0.001	0.001	0.001	0.001	0.001	0.001	0.001	0.001	0.001
V	0.000	0.000	0.000	0.000	0.000	0.000	0.000	0.000	0.000	0.000	0.000	0.000	0.000	0.000	0.000	0.000	0.000
Mn	0.001	0.001	0.001	0.001	0.001	0.001	0.001	0.001	0.001	0.001	0.001	0.001	0.001	0.001	0.001	0.001	0.001
Fe	0.055	0.059	0.059	0.058	0.074	0.074	0.074	0.074	0.074	0.072	0.074	0.075	0.075	0.075	0.076	0.076	0.075
Zn	0.002	0.002	0.002	0.002	0.001	0.001	0.001	0.001	0.001	0.001	0.001	0.001	0.001	0.001	0.001	0.001	0.001
Rb	0.000	0.000	0.000	0.000	0.000	0.000	0.000	0.000	0.000	0.000	0.000	0.000	0.000	0.000	0.000	0.000	0.000
Cs	0.002	0.002	0.002	0.002	0.002	0.002	0.002	0.002	0.002	0.003	0.002	0.002	0.002	0.002	0.002	0.002	0.002

Table A4. *Cont.*

	MG-14	MG-15	NA-1	NA-2	NA-3	NA-4	NA-5	NA-6	NA-7	NA-8	NA-9	NA-10	NA-11	NA-12	NA-13	NA-14	NA-15	DL
Li	134	139	563	561	540	542	573	548	527	558	537	578	578	538	537	555	564	0.4
Na	1710	1796	8658	8691	8469	8587	8854	8731	8860	8870	8855	8886	8996	8850	8683	8806	8832	0.4
Mg	229.4	230.2	5102	5122	5099	5203	5263	5181	5232	5310	5210	5261	5322	5303	5266	5210	5265	0.06
K	50.4	49.2	639	641	560	560.4	664	644	635	659	633	643	670	658	615	654	649	0.15
Sc	3.80	3.40	549	553	539	537	544	550	557	556	542	547	551	555	548	552	574	0.2
Ti	68.1	68.4	87.8	85.2	87.8	77.3	81.1	81.2	83.9	77.0	83.4	81.6	86.8	83.1	78.5	81.0	80.1	1.3
V	7.41	7.74	61.5	61.0	61.0	62.3	63.2	62.7	63.2	63.2	62.9	62.8	66.0	64.9	63.3	63.9	65.1	0.001
Mn	117	119	338	330	332	314	340	342	339	355	294	332	343	349	302	318	320	0.01
Fe	7620	7696	15,800	15,686	15,631	15,650	15,748	15,771	15,898	15,958	15,798	15,918	16,145	16,220	15,896	15,988	16,100	0.05
Zn	86.7	87.7	84.8	87.4	87.9	85.5	88.0	87.6	90.3	86.7	86.3	90.5	86.5	87.4	82.8	84.3	88.4	0.02
Rb	421.0	44.0	89.7	88.5	87.5	87.4	89.8	90.1	92.0	91.0	91.4	92.5	93.4	94.1	90.9	93.7	93.8	0.003
Cs	550	549	696	706	692	691	750	712	724	712	716	719	717	716	683	711	718	0.001
cation (apfu)																		
Li	0.011	0.011	0.047	0.047	0.046	0.046	0.048	0.046	0.044	0.046	0.046	0.049	0.048	0.045	0.045	0.047	0.047	
Na	0.041	0.044	0.217	0.218	0.215	0.219	0.226	0.221	0.226	0.223	0.227	0.226	0.226	0.225	0.220	0.224	0.223	
Mg	0.005	0.005	0.121	0.121	0.123	0.125	0.127	0.124	0.126	0.126	0.126	0.127	0.127	0.127	0.126	0.125	0.126	
K	0.001	0.001	0.009	0.009	0.008	0.008	0.010	0.010	0.010	0.010	0.010	0.010	0.010	0.010	0.009	0.010	0.010	
Sc	0.000	0.000	0.007	0.007	0.007	0.007	0.007	0.007	0.007	0.007	0.007	0.007	0.007	0.007	0.007	0.007	0.007	
Ti	0.001	0.001	0.001	0.001	0.001	0.001	0.001	0.001	0.001	0.001	0.001	0.001	0.001	0.001	0.001	0.001	0.001	
V	0.000	0.000	0.001	0.001	0.001	0.001	0.001	0.001	0.001	0.001	0.001	0.001	0.001	0.001	0.001	0.001	0.001	
Mn	0.001	0.001	0.004	0.003	0.004	0.003	0.004	0.004	0.004	0.004	0.003	0.004	0.004	0.004	0.003	0.003	0.003	
Fe	0.076	0.077	0.163	0.162	0.164	0.164	0.165	0.164	0.167	0.165	0.167	0.167	0.167	0.169	0.166	0.167	0.167	
Zn	0.001	0.001	0.001	0.001	0.001	0.001	0.001	0.001	0.001	0.001	0.001	0.001	0.001	0.001	0.001	0.001	0.001	
Rb	0.000	0.000	0.001	0.001	0.001	0.001	0.001	0.001	0.001	0.001	0.001	0.001	0.001	0.001	0.001	0.001	0.001	
Cs	0.002	0.002	0.003	0.003	0.003	0.003	0.003	0.003	0.003	0.003	0.003	0.003	0.003	0.003	0.003	0.003	0.003	

References

1. Daneshvar, N.; Azizi, H.; Asahara, Y.; Tsuboi, M.; Minami, M.; Mohammad, Y.O. Geochemistry and Genesis of Beryl Crystals in the LCT Pegmatite Type, Ebrahim-Attar Mountain, Western Iran. *Minerals* **2021**, *11*, 717. [CrossRef]
2. Wang, P.; Gray, T.P.; Li, Z.; Anderson, E.J.D.; Allaz, J.; Smyth, J.R.; Koenig, A.E.; Qi, L.j.; Zhou, Y.; Raschke, M.B. Mineralogical classification and crystal water characterisation of beryl from the W–Sn–Be occurrence of Xuebaoding, Sichuan province, western China. *Mineral. Mag.* **2021**, *85*, 172–188. [CrossRef]
3. Černý, P. Mineralogy of Beryllium in Granitic Pegmatites. *Rev. Mineral. Geochem.* **2002**, *50*, 405–444. [CrossRef]
4. Aurisicchio, C.; Fioravanti, G.; Grubessi, O.; Zanazzi, P.F. Reappraisal of the crystal chemistry of beryl. *Am. Miner.* **1988**, *73*, 826–837.
5. Wood, D.L.; Nassau, K. Infrared Spectra of Foreign Molecules in Beryl. *J. Chem. Phys.* **1967**, *47*, 2220–2228. [CrossRef]
6. Yu, X.Y. *Colored Gemmology*, 2nd ed.; Geological Publishing House: Beijing, China, 2019; pp. 150–151.
7. Shen, J.Q.; Hu, Z.K.; Cui, S.Y.; Zhang, Y.F.; Li, E.Q.; Liang, W.; Xu, B. A Study on Beryl in the Cuonadong Be-W-Sn Polymetallic Deposit, Longzi County, Tibet, China. *Crystals* **2021**, *11*, 777. [CrossRef]
8. Bhandari, S.; Qin, K.; Zhou, Q.; Evans, N.J. Geological, Mineralogical and Geochemical Study of the Aquamarine-Bearing Yamrang Pegmatite, Eastern Nepal with Implications for Exploration Targeting. *Minerals* **2022**, *12*, 564. [CrossRef]
9. Hoyer, I.d.S.; Souza, V.d.S.; Debowski, B.P. Aquamarine from Massangana batholith, Rondônia State: Mineral chemistry and fluid inclusion data. *REM-Int. Eng. J.* **2020**, *73*, 319–327. [CrossRef]
10. Groat, L.A.; Giuliani, G.; Stone-Sundberg, J.; Sun, Z.; Renfro, N.D.; Palke, A.C. A Review of Analytical Methods Used in Geographic Origin Determination of Gemstones. *Gems Gemol.* **2019**, *55*, 512–535. [CrossRef]
11. Xu, B.; Hou, Z.-Q.; Griffin, W.L.; Lu, Y.; Belousova, E.; Xu, J.-F.; O'Reilly, S.Y. Recycled volatiles determine fertility of porphyry deposits in collisional settings. *Am. Mineral.* **2021**, *106*, 656–661. [CrossRef]
12. Xu, B.; Hou, Z.-Q.; Griffin, W.L.; O'Reilly, S.Y.; Zheng, Y.-C.; Wang, T.; Bin, F.; Xu, J.-F. In-situ mineralogical interpretation of the mantle geophysical signature of the Gangdese Cu-porphyry mineral system. *Gondwana Res.* **2022**, *111*, 53–63. [CrossRef]
13. Xu, B.; Hou, Z.-Q.; Griffin, W.L.; Zheng, Y.-C.; Wang, T.; Guo, Z.; Hou, J.; Santosh, M.; O'Reilly, S.Y. Cenozoic lithospheric architecture and metallogenesis in Southeastern Tibet. *Earth-Sci. Rev.* **2021**, *214*, 103472. [CrossRef]
14. Xu, B.; Hou, Z.-Q.; Griffin, W.L.; Yu, J.-X.; Long, T.; Zhao, Y.; Wang, T.; Fu, B.; Belousova, E.; O'Reilly, S.Y. Apatite halogens and Sr-O and zircon Hf-O isotopes: Recycled volatiles in Jurassic porphyry ore systems in southern Tibet. *Chem. Geol.* **2022**, *605*, 120924. [CrossRef]
15. Xu, B.; Griffin, W.L.; Xiong, Q.; Hou, Z.-Q.; O'Reilly, S.Y.; Guo, Z.; Pearson, N.J.; Gréau, Y.; Yang, Z.-M.; Zheng, Y.-C. Ultrapotassic rocks and xenoliths from South Tibet: Contrasting styles of interaction between lithospheric mantle and asthenosphere during continental collision. *Geology* **2017**, *45*, 51–54. [CrossRef]
16. Saeseaw, S.; Renfro, N.D.; Palke, A.C.; Sun, Z.; McClure, S.F. Geographic Origin Determination of Emerald. *Gems Gemol.* **2019**, *55*, 614–646. [CrossRef]
17. Palke, A.C.; Saeseaw, S.; Renfro, N.D.; Sun, Z.; McClure, S.F. Geographic Origin Determination of Ruby. *Gems Gemol.* **2019**, *55*, 580–613. [CrossRef]
18. Palke, A.C.; Saeseaw, S.; Renfro, N.D.; Sun, Z.; McClure, S.F. Geographic Origin Determination of Blue Sapphire. *Gems Gemol.* **2019**, *55*, 536–579. [CrossRef]
19. Fukuda, J.; Shinoda, K. Water molecules in beryl and cordierite: High-temperature vibrational behavior, dehydration, and coordination to cations. *Phys. Chem. Miner.* **2011**, *38*, 469–481. [CrossRef]
20. Hu, Y.; Lu, R. Color Characteristics of Blue to Yellow Beryl from Multiple Origins. *Gems Gemol.* **2020**, *56*, 54–65. [CrossRef]
21. Zhou, Q.; Qin, K.; Tang, D.; Wang, C.; Tian, Y.; Sakyi, P.A. Mineralogy of the Koktokay No. 3 pegmatite, Altai, NW China: Implications for evolution and melt–fluid processes of rare-metal pegmatites. *Eur. J. Mineral.* **2015**, *27*, 433–457. [CrossRef]
22. Pedrosa-Soares, A.C.; De Campos, C.P.; Noce, C.; Silva, L.C.; Novo, T.; Roncato, J.; Medeiros, S.; Castañeda, C.; Queiroga, G.; Dantas, E.; et al. Late Neoproterozoic-Cambrian granitic magmatism in the Araçuaí orogen (Brazil), the Eastern Brazilian Pegmatite Province and related mineral resources. *Geol. Soc. Lond. Spec. Publ.* **2022**, *350*, 25–51. [CrossRef]
23. Ballouard, C.; Elburg, M.A.; Tappe, S.; Reinke, C.; Ueckermann, H.; Doggart, S. Magmatic-hydrothermal evolution of rare metal pegmatites from the Mesoproterozoic Orange River pegmatite belt (Namaqualand, South Africa). *Ore Geol. Rev.* **2020**, *116*, 103252. [CrossRef]
24. Wen, L.; Liang, W.X.; Zhang, Z.G.; Huang, J.C. *The Infrared Spectroscopy of Minerals*; Chongqing University Press: Chongqing, China, 1988; pp. 79–81.
25. Aurisicchio, C.; Grubessi, O.; Zecchini, P. Infrared spectroscopy and crystal chemistry of the beryl group. *Can. Mineral.* **1994**, *32*, 55–68.
26. Zhou, K.C.; Qi, L.J.; Xiang, C.J. Study on gemology of beryl gem from Pingwu Sichuan and mechanism of irradiation inducing coloration. *China Min. Mag.* **2005**, *14*, 30–32.
27. Jehlička, J.; Culka, A.; Bersani, D.; Vandenabeele, P. Comparison of seven portable Raman spectrometers: Beryl as a case study. *J. Raman Spectrosc.* **2017**, *48*, 1289–1299. [CrossRef]
28. Pisutha-Arnond, V.; Atichat, W.; Nhung, N.T.; Khoi, N.N.; Häger, T.; Hofmeister, W.; Huong, L.T.-T. Aquamarine from the Thuong Xuan District, Thanh Hoa Province, Vietnam. *Gems Gemol.* **2011**, *47*, 42–48. [CrossRef]

29. Sardi, F.G.; Heimann, A. Pegmatitic Beryl as Indicator of Melt Evolution: Example from the Velasco District, Pampeana Pegmatite Province, Argentina, and Review of Worldwide Occurrences. *Can. Mineral.* **2014**, *52*, 809–836. [CrossRef]
30. Hamis, A.; Kesraoui, M.; Boutaleb, A.; Fuchs, Y.; Marignac, C. Beryl occurrences in the granitic complex of Guerioune, Laouni, Southeastern Algeria: Electron microprobe, infrared spectroscopy, and fluid inclusions data. *Arab. J. Geosci.* **2021**, *14*, 357. [CrossRef]
31. Borzenko, A.A.; Yurgenson, G.A. Scandium, Yttrium and Lanthanids in the Beryl of the Sherlovaya Gora Deposit. In *Minerals: Structure, Properties, Methods of Investigation. Springer Proceedings in Earth and Environmental Sciences*; Springer: Cham, Switzerland, 2020; pp. 37–42. [CrossRef]
32. Rossman, G.R. Color in Gems: The New Technologies. *Gems Gemol.* **1981**, *17*, 60–71. [CrossRef]
33. Goldman, D.S.; Rossman, G.R.; Parkin, K.M. Channel constituents in beryl. *Phys. Chem. Miner.* **1978**, *3*, 225–235. [CrossRef]
34. Viana, R.R.; da Costa, G.M.; De Grave, E.; Stern, W.B.; Jordt-Evangelista, H. Characterization of beryl (aquamarine variety) by Mösssbauer spectroscopy. *Phys. Chem. Miner.* **2002**, *29*, 78–86. [CrossRef]
35. Taran, M.N.; Rossman, G.R. Optical spectroscopic study of tuhualite and a re-examination of the beryl, cordierite, and osumilite spectra. *Am. Mineral.* **2001**, *86*, 937–980. [CrossRef]
36. Lum, J.E.; Viljoen, F.; Cairncross, B.; Frei, D. Mineralogical and geochemical characteristics of BERYL (AQUAMARINE) from the Erongo Volcanic Complex, Namibia. *J. Afr. Earth Sci.* **2016**, *124*, 104–125. [CrossRef]
37. Merino, E.; Villaseca, C.; Orejana, D.; Jeffries, T. Gahnite, chrysoberyl and beryl co-occurrence as accessory minerals in a highly evolved peraluminous pluton: The Belvís de Monroy leucogranite (Cáceres, Spain). *Lithos* **2013**, *179*, 137–156. [CrossRef]
38. Ding, P. Study on Mineralogical Characteristic and Fluid Inclusions of Aquamarine from Fugong, Yunnan Province. Master's Thesis, China University of Geosciences, Beijing, China, 2012.
39. Fridrichová, J.; Bačík, P.; Rusinová, P.; Antal, P.; Škoda, R.; Bizovská, V.; Miglierini, M. Optical and crystal-chemical changes in aquamarines and yellow beryls from Thanh Hoa province, Vietnam induced by heat treatment. *Phys. Chem. Miner.* **2014**, *42*, 287–302. [CrossRef]
40. Groat, L.A.; Rossman, G.R.; Dyar, M.D.; Turner, D.; Piccoli, P.M.B.; Schultz, A.J.; Ottolini, L. Crystal Chemistry of Dark Blue Aquamarine from the True Blue Showing, Yukon Territory, Canada. *Can. Mineral.* **2010**, *48*, 597–613. [CrossRef]
41. Beal, K.L.; Lentz, D.R. Aquamarine beryl from Zealand Station, Canada: A mineralogical and stable isotope study. *J. Geosci.* **2012**, *55*, 57–67. [CrossRef]
42. Kim, S.J.; Shin, D.W.; Shon, S.H.; Jang, Y.D. Gemological Characteristics of Aquamarine from the Gilgit-Baltistan of Northern Areas, Pakistan. *J. Mineral. Soc. Korea* **2015**, *28*, 51–60. [CrossRef]
43. Bocchio, R.; Adamo, I.; Caucia, F. Aquamarine from the Masino-Bregaglia Massif, Central Alps, Italy. *Gems Gemol.* **2009**, *45*, 204–207. [CrossRef]

Disclaimer/Publisher's Note: The statements, opinions and data contained in all publications are solely those of the individual author(s) and contributor(s) and not of MDPI and/or the editor(s). MDPI and/or the editor(s) disclaim responsibility for any injury to people or property resulting from any ideas, methods, instructions or products referred to in the content.